Journal of
Materials Chemistry A

ROYAL SOCIETY
OF CHEMISTRY

PAPER

View Article Online
View Journal | View Issue

Cite this: *J. Mater. Chem. A*, 2026, **14**, 20519

Synergistic Cu/F co-doped P2-$Na_{0.67}Ni_{0.33}Mn_{0.67}O_2$ microsphere cathodes for enhanced sodium storage *via* dual doping and structural design

Mengfei Wu, Huaao Li, Ao Liu, Tianci Sun and Yifan Dong *

Received 26th January 2026
Accepted 13th April 2026

DOI: 10.1039/d6ta00731g

rsc.li/materials-a

The development of high-performance cathode materials is crucial for advancing sodium-ion batteries (SIBs). P2-type layered transition-metal oxides are promising cathode candidates, yet they suffer from capacity fading and poor rate performance, primarily due to irreversible phase transitions, Jahn–Teller distortion, and interfacial side reactions. To address these challenges, we report a Cu/F co-doped P2-$Na_{0.67}Ni_{0.33}Mn_{0.67}O_2$ cathode with a unique microsphere architecture. The microsphere structure reduces interfacial side reactions, while the synergistic effect of co-doping plays a key role: the Cu^{2+}/Cu^{3+} redox couple elevates the operating voltage, and F^- doping enhances lattice stability and suppresses Jahn–Teller distortion. The optimized electrode delivers a high specific capacity of 139.6 mA h g^{-1} at 0.1C and exhibits excellent cycling stability with 88.07% capacity retention after 100 cycles at 1C. *In situ* XRD reveals a highly reversible solid-solution reaction with a minimal volume change of only 1.5%. This comprehensive modification strategy provides a new avenue for designing high-stability layered oxide cathodes suitable for practical sodium-ion batteries.

1. Introduction

The escalating global energy crisis necessitates an urgent transition to sustainable energy solutions.[1] Sodium-ion batteries (SIBs) have emerged as a promising alternative to lithium-ion batteries (LIBs), owing to the abundant availability and cost-effectiveness of sodium resources.[2,3] The overall performance of SIBs is largely determined by their cathode materials.[4] Therefore, the development of cathode materials with high energy density and superior electrochemical performance is of critical importance for advancing sodium-ion battery technology.[5]

Currently, a variety of cathode materials for sodium-ion batteries have been developed, primarily including polyanion-type compounds,[6,7] Prussian blue analogues,[8,9] organic compounds,[10,11] and layered transition metal oxides.[12,13] Among them, P2-type layered transition metal oxides have garnered significant research interest owing to their high reversible capacity and relatively straightforward synthesis.[14] However, several intrinsic issues-such as the Jahn–Teller distortion, interfacial side reactions, and complex phase transitions induced by interlayer gliding collectively result in rapid capacity fading and limited rate capability in these layered oxide cathodes.[15–18]

To address the aforementioned challenges, various modification strategies have been developed. For instance, Fang *et al.*[19] synthesized uniform P2-$Na_{0.7}CoO_2$ microspheres. This distinctive spherical morphology exhibits a reduced specific surface area, which minimizes the contact interface between the active material and the electrolyte, thereby effectively suppressing interfacial side reactions. In another approach, Cui *et al.*[20] introduced Mg into the Na layer of a P2-type cathode. The formed Mg–TM dimers within the Na layer help to inhibit irreversible phase transitions and enhance structural stability. Furthermore, the incorporation of highly electronegative fluorine modifies the electronic environment of oxygen, altering O–O and TM–O bond energies. This results in a contraction of atomic spacing while expanding the interlayer distance, which accelerates Na^+ diffusion and mitigates lattice distortion induced by the Jahn–Teller effect. However, there is currently no method that can simultaneously suppress interfacial side reactions and the Jahn–Teller effect.

In this study, a Cu/F co-doped P2-$Na_{0.67}Ni_{0.23}Mn_{0.67}Cu_{0.1}O_{1.9}F_{0.1}$ microsphere was synthesized. The unique microsphere architecture effectively reduces the specific surface area of the material, thereby minimizing the contact interface between the active material and the electrolyte. This reduction suppresses detrimental interfacial side reactions and mitigates the dissolution of active species, leading to significantly enhanced coulombic efficiency. Cu^{2+} exhibits intrinsic electrochemical activity. In contrast to other electrochemically inert dopants, the Cu^{2+}/Cu^{3+} redox couple contributes an elevated operating potential to copper-substituted cathode materials. Concurrently, the introduction of F^- enhances structural stability through multiple mechanisms: the stronger TM–F bond

---

State Key Laboratory of Biogeology and Environmental Geology, China University of Geosciences, Wuhan, China. E-mail: dongyf@cug.edu.cn

compared to TM–O increases the cation–anion interaction, thereby suppressing irreversible oxygen loss during cycling. Furthermore, fluorine substitution for oxygen disrupts the symmetry of the TMO$_6$ octahedra, which mitigates Jahn–Teller distortion and helps maintain structural integrity.

The assembled half-cell delivered a remarkable discharge specific capacity of 139.6 mA h g^{-1} within the 2.0–4.4 V window at 0.1C, and maintained an impressive 88.07% capacity retention after 100 cycles at 1C. *In situ* XRD analysis further demonstrated exceptional structural integrity, confirming that the P2 phase remained stable throughout cycling with a remarkably small volume change of merely 1.5% and no detectable irreversible phase transition. This combined modification strategy represents a promising and effective approach for designing advanced layered cathode materials with superior electrochemical performance.

2. Experimental section

2.1 Materials synthesis

The precursors were synthesized *via* a coprecipitation method. A certain proportion of NiSO$_4$·6H$_2$O, MnSO$_4$·H$_2$O and CuSO$_4$·5H$_2$O were dissolved in distilled water to form 2 M sulfate solution. Use a 1.4 M aqueous solution of Na$_2$CO$_3$ as the precipitating agent, and a 2.5 M aqueous solution of NH$_4$HCO$_3$ as the auxiliary precipitating agent. The reaction was conducted at room temperature by simultaneously adding the three liquid precursors to the flask. The mixture was continuously stirred at 800 rpm for 55 hours. After the reaction, the carbonate precursor was obtained by centrifugation, washing and drying. $Na_{0.67}Ni_{0.33-x}Mn_{0.67}Cu_xO_2$ ($x = 0, 0.05, 0.1, 0.15$) was prepared by a traditional solid method. The precursor and Na$_2$CO$_3$ (excess 5 wt%) were weighed according to the stoichiometric ratio, and then mixed and ground in a mortar for 1 h. The mixed powder was then placed in a muffle furnace and calcined at 450 °C for 6 h and then calcined at 950 °C for 15 h to obtain $Na_{0.67}Ni_{0.33-x}Mn_{0.67}Cu_xO_2$. The precursor, Na$_2CO_3$ (excess 5 wt%) and NaF (excess 5 wt%) were mixed and ground in a certain proportion, calcined at 450 °C for 6 h and then calcined at 950 °C for 15 h to obtain $Na_{0.67}Ni_{0.23}Mn_{0.67}Cu_{0.1}O_{2-y}F_y$.

2.2 Material characterization

The crystal structure of the samples was characterized using X-ray diffraction (XRD; Rigaku Smart Lab SE). The measurements were performed in a 2θ range from 10° to 80° with a scanning speed of 1° min^{-1}. The surface morphology was examined using a field-emission scanning electron microscope (FE-SEM; Hitachi SU8010). Elemental identification was conducted with an energy-dispersive X-ray spectrometer (EDS) attached to the microscope. The chemical composition and stoichiometry were analyzed by X-ray photoelectron spectroscopy (XPS) using a Thermo Scientific K-Alpha instrument with a monochromatic Al Kα X-ray source.

2.3 Electrochemical measurements

The as-prepared active material, Super P carbon black, and polyvinylidene fluoride (PVDF) were mixed at a mass ratio of 8 : 1 : 1 and ground using *N*-methyl-2-pyrrolidone (NMP) as a solvent. The resulting slurry was uniformly coated onto carbon-coated aluminum foil using a doctor blade, followed by drying at 80 °C for 12 hours in a vacuum oven. The dried electrodes were then punched into 12 mm diameter circular discs. Sodium half-cells were assembled using a sodium metal counter/reference electrode, a Whatman GF/A glass fiber separator, and an electrolyte of 1 M sodium perchlorate (NaClO$_4$) in a mixture of propylene carbonate (PC) and fluoroethylene carbonate (FEC) (95 : 5 by volume). Galvanostatic charge/discharge tests and the galvanostatic intermittent titration technique (GITT) were performed using a Land test system. Cyclic voltammetry (CV) was conducted on a CHI 760E electrochemical workstation. The GITT measurements involved a 10-minute charging pulse followed by a 30-minute relaxation period. The sodium-ion diffusion coefficient (D) was calculated based on Fick's second law and the corresponding boundary conditions, using the following formula:

$$D = \frac{4}{\pi\tau}\left(\frac{n_m V_m}{S}\right)^2\left[\frac{\Delta E_S}{\Delta E_t}\right]^2$$

where D is the sodium-ion diffusion coefficient, τ is the relaxation time, n_m is the number of moles of sodium ions, V_m is the molar volume of the electrode material, S is the contact area between the electrode and electrolyte, ΔE_S is the steady-state voltage change over the entire pulse step, and ΔE_t is the voltage change during the constant-current pulse. Cyclic voltammetry (CV) was employed to investigate the redox characteristics and kinetic processes of the material. This technique involves applying a linearly varying potential and measuring the resulting current response. The sodium-ion diffusion coefficient was further calculated using the Randles–Sevcik equation, which describes the linear relationship between the peak current and the square root of the scan rate:

$$I_p = 26\,900 n^{\frac{3}{2}} A C D^{\frac{1}{2}} V^{\frac{1}{2}}$$

In this equation, I_p represents the peak current, n_m is the number of electrons transferred in the redox reaction, A is the electroactive surface area, C is the bulk concentration of sodium ions, D is the diffusion coefficient, and V is the potential scan rate.

3. Results and discussion

A series of $Na_{0.67}Ni_{0.33-x}Mn_{0.67}Cu_xO_2$ ($x = 0, 0.05, 0.1, 0.15$) microspheres with varying copper contents were synthesized *via* a coprecipitation method, and an optimal doping ratio was subsequently determined. The crystal structure of the samples was analyzed using X-ray diffraction (XRD), as shown in Fig. 1a. The results reveal that all samples exhibit highly intense and sharp diffraction peaks, which can be indexed to the P2-type structure with the space group $P6_3/mmc$.[21] Rietveld refinement was further performed on the XRD data (Fig. 1b, c and S1). The refinement results indicate that the *c*-axis parameter gradually increases with higher Cu content (Table S1). This expansion can be attributed to the larger ionic radius of Cu^{2+} (72 pm) compared with that of Ni^{2+} (69 pm). Morphology characterization was carried out by scanning electron microscopy (SEM). As displayed in Fig. S2, the samples present a soccer-ball-like shape. Energy-dispersive spectroscopy (EDS) mapping clearly demonstrates the homogeneous distribution of Na, Ni, Mn, Cu, and O throughout the sample (Fig. 1d and S3).

To determine the optimal copper doping level, the electrochemical performance of the sodium half-cells was evaluated through cycling tests at various rates and galvanostatic intermittent titration technique (GITT) measurements at room temperature. As shown in Fig. 1e, within a voltage window of 2.0–4.4 V at a current density of 1C (170 mA g^{-1}), the undoped sample $Na_{0.67}Ni_{0.33}Mn_{0.67}O_2$ (NNM) delivered the highest initial discharge capacity of 129.3 mA h g^{-1}. The introduction of Cu led to a reduction in the initial specific capacity, which can be attributed to two primary factors. First, the substitution of Ni (atomic weight 58.69) by Cu (atomic weight 63.55) increases the formula weight of the material, thereby lowering its theoretical specific capacity. Second, during the charge–discharge process, redox reactions involve the Cu^{2+}/Cu^{3+} and $Ni^{2+}/Ni^{3+}/Ni^{4+}$ couples. As each Cu ion transfers only half the number of electrons per mole compared to Ni, the amount of extractable Na^+ is correspondingly reduced in Cu-doped samples.[22] After 100 cycles, the NNM electrode retained only 48.88% of its initial capacity. In contrast, Cu doping significantly improved cycling stability, with the $Na_{0.67}Ni_{0.23}Mn_{0.67}Cu_{0.1}O_2$ (NNMC10) sample exhibiting a capacity retention of 80.64%, representing an enhancement of 31.76 percentage points. This improvement is ascribed to the electrochemically active Cu^{2+}/Cu^{3+} redox couple, which operates at a higher potential and contributes to structural stabilization during cycling, as evidenced by the superior capacity retention at high voltages.[23] The Na^+ diffusion coefficients, calculated from GITT data (Fig. 1f and g), further

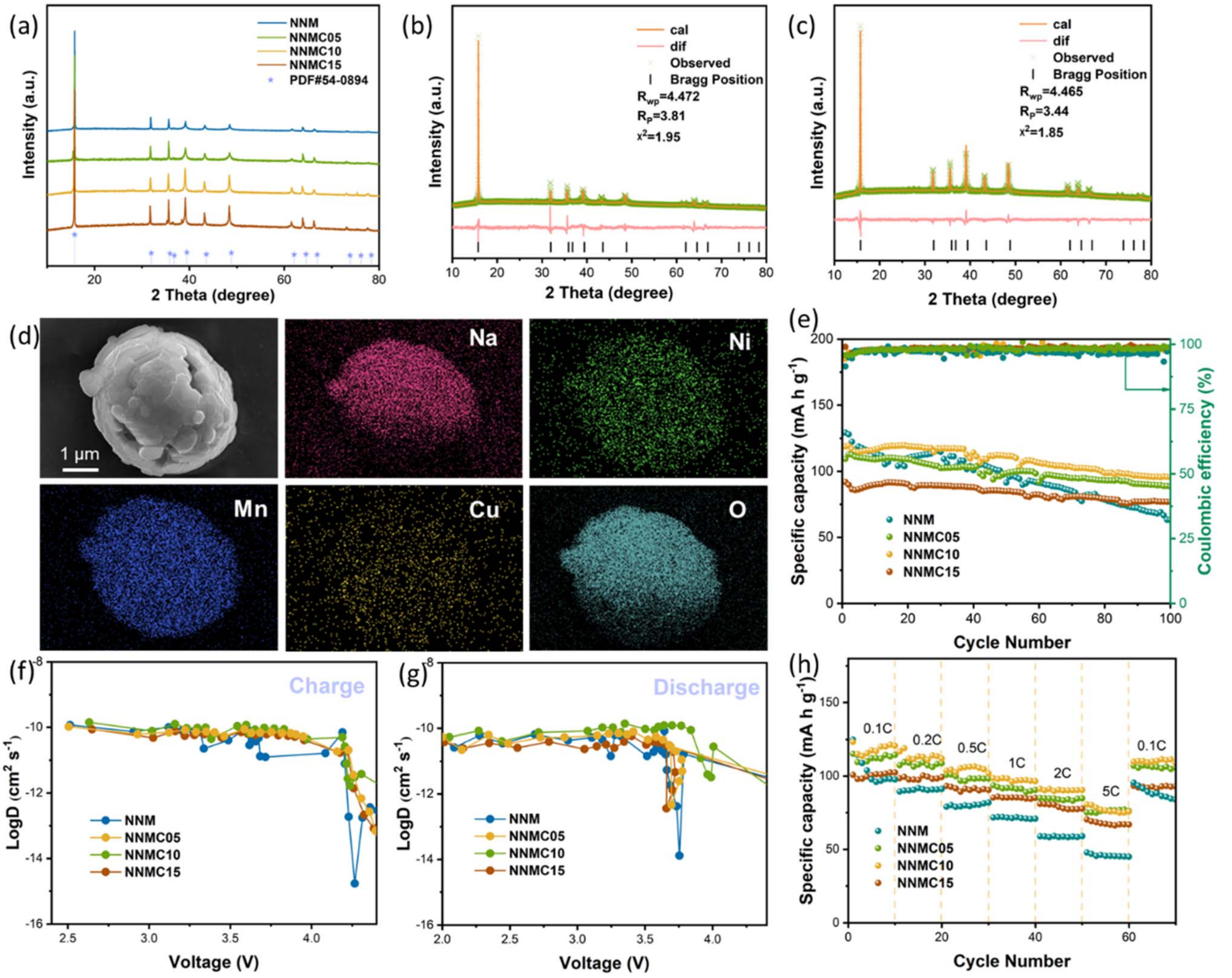

Fig. 1 (a) XRD patterns of samples with different Cu doping concentrations. Rietveld refined XRD pattern of (b) NNM and (c) NNMC10. (d) Energy dispersive spectroscopy (EDS) elemental maps of NNMC10. The electrochemical performance of samples at a voltage range of 2–4.4 V (e) cycling performance at 1C for 100 cycles, (f) the Na^+ diffusion rate during the charging process calculated through the GITT test, (g) the diffusion rate of Na^+ during the discharge process and (h) rate performance at 0.1–5 C.

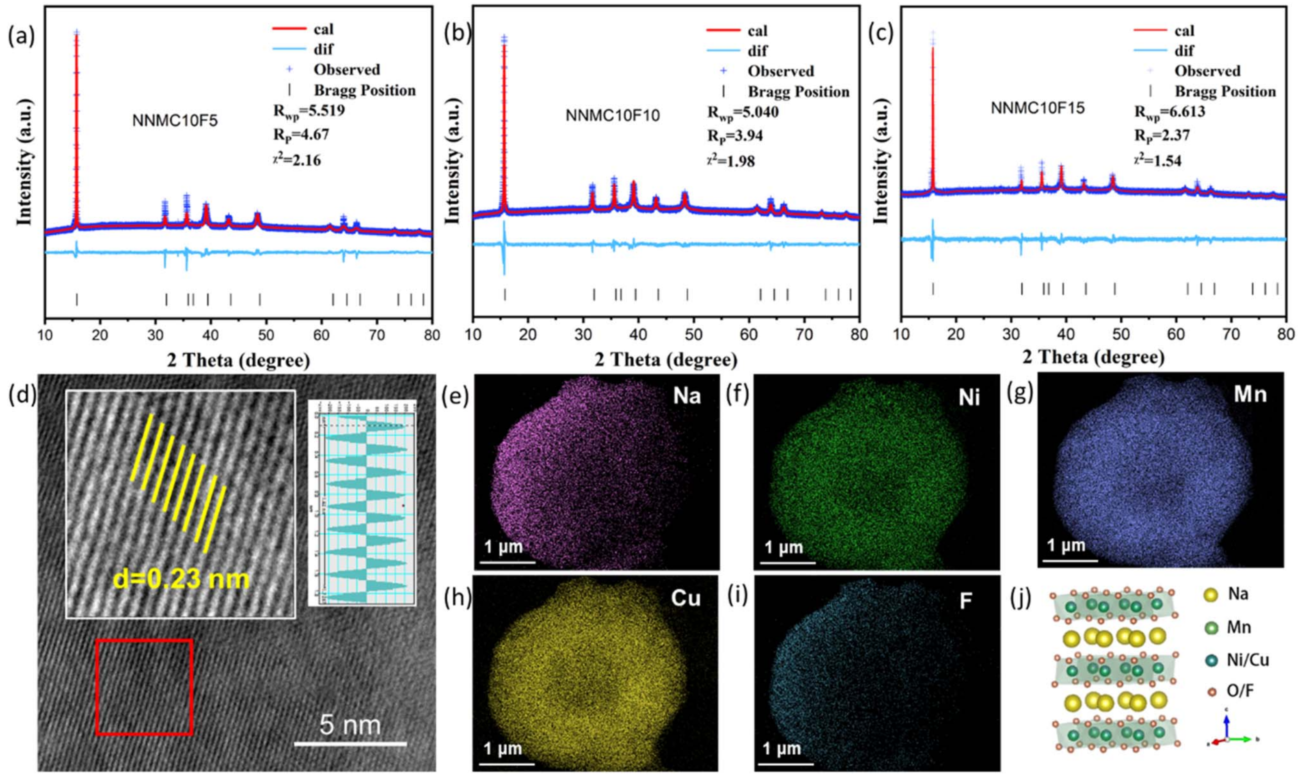

Fig. 2 Rietveld refined XRD pattern of (a) NNMC10F5, (b) NNMC10F10 and (c) NNMC10F15. (d) HRTEM image of NNMC10F10. Energy dispersive spectroscopy (EDS) elemental mapping. (e–i) Sodium, nickel, manganese, copper and fluorine are all uniformly distributed in the entire sample. (j) Schematic diagram of the crystal structure with Cu/F doping.

elucidate the kinetic properties. The NNMC10 electrode demonstrated the highest Na$^+$ diffusion coefficient, ranging from 10^{-12} to 10^{-10} cm^2 s^{-1}, which is substantially greater than that of the NNM sample (10^{-15} to 10^{-10} cm^2 s^{-1}). These GITT results indicate that the NNMC10 composition possesses the most favorable ionic conductivity and rate capability, consistent with its rate performance shown in Fig. 1h. Notably, even at a high current density of 5C, the NNMC10 electrode maintained a first-cycle discharge capacity of 80.6 mA h g^{-1}.

Based on the aforementioned results, the sample with a Cu^{2+} doping level of 0.1 ($Na_{0.67}Ni_{0.23}Mn_{0.67}Cu_{0.1}O_2$) exhibits the best overall performance among the studied series. However, the enhancement in capacity and cycling stability, while significant, remains limited for practical application. To further improve the electrochemical properties, we introduced fluorine (F$^-$) as an anionic dopant with varying concentrations into the optimized Cu-doped structure. Scanning electron microscopy (SEM) images (Fig. S4) reveal that fluorine doping does not compromise the spherical morphology of the as-synthesized microspheres. To further investigate the microstructure, high-resolution transmission electron microscopy (HR-TEM) was conducted on $Na_{0.67}Ni_{0.23}Mn_{0.67}Cu_{0.1}O_{1.9}F_{0.1}$ (NNMC10F10) (Fig. 2d), revealing distinct lattice fringes with a spacing of 0.23 nm, which corresponds to the (012) crystal plane identified from the XRD refinement. EDS elemental mapping (Fig. 2e–i) further confirms the homogeneous distribution of Na, Ni, Cu, Mn and F throughout the material. The crystal structure of the F-doped samples was examined by X-ray diffraction (XRD), and the patterns were refined using the Rietveld method (Fig. 2a–c). All diffraction patterns correspond well to a P2-type layered structure with the $P6_3/mmc$ space group. No secondary phases were detected within the resolution of XRD, confirming that fluorine incorporation preserves the desired host structure. The Rietveld refinement reliability factors (R_{wp} and R_p), summarized in Table S2, are all below 10%, confirming the high quality of the structural models. The refined lattice parameters reveal a non-monotonic variation in the a-axis with increasing F$^-$ content: it initially contracts and subsequently expands. The initial contraction is attributed to the substitution of larger O^{2-} ions (140 pm) by smaller F$^-$ ions (136 pm), coupled with the high electronegativity of fluorine, which strengthens the metal–anion bonds.[24] However, further F$^-$ doping increases the proportion of Mn^{3+} (64.5 pm) relative to Mn^{4+} (53 pm) due to charge compensation.[25] The larger ionic radius of Mn^{3+} subsequently causes the a-axis to expand, explaining the observed trend. A schematic of the crystal structure is presented in Fig. 2j. In addition, Brunauer–Emmett–Teller (BET) measurements (Table S3) show that the spherical morphology results in a relatively low specific surface area. This surface area is further reduced upon co-doping with Cu and F. A smaller electrode–electrolyte contact area helps mitigate interfacial side reactions, thereby effectively improving the cycling stability of the material.[26]

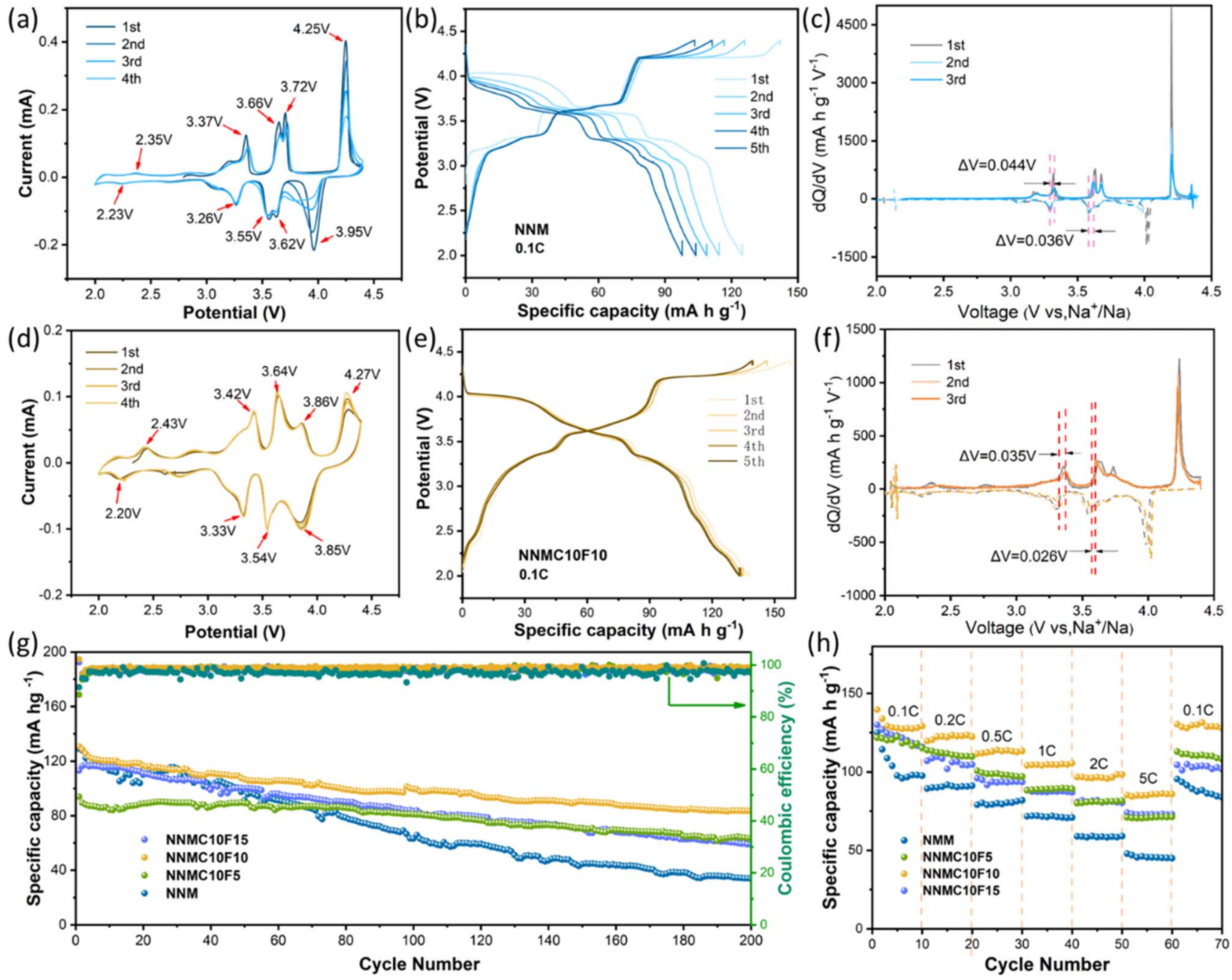

Fig. 3 The electrochemical performance of NNM (a) CV curves at 0.1 mV s^{-1}, (b) charge–discharge curves and (c) d*Q*/d*V* curves. The electrochemical performance of NNMC10F10 (d) CV curves at 0.1 mV s^{-1}, (e) charge–discharge curves and (f) d*Q*/d*V* curves. (g) Cycling performance at 1C between 2.0 and 4.4 V of the four cathode materials. (h) Rate capability.

The electrochemical performance of the samples was evaluated within a voltage window of 2.0–4.4 V. Cyclic voltammetry (CV) was employed to compare the Na^+ storage behavior of the NNM and NNMC10F10 materials. Fig. 3a and d present the CV curves obtained at a scan rate of 0.1 mV s^{-1}. For the NNM sample (Fig. 3a), five distinct redox couples are observed at approximately 2.35/2.23 V, 3.37/3.26 V, 3.66/3.55 V, 3.72/3.62 V, and 4.25/3.95 V, corresponding to the voltage plateaus in its galvanostatic charge–discharge profile. The pair at 2.35/2.23 V is assigned to the Mn^{3+}/Mn^{4+} redox reaction. The subsequent three pairs are attributed to the multi-step $Ni^{2+}/Ni^{3+}/Ni^{4+}$ redox process, concomitant with Na^+/vacancy ordering.[27] The redox couple beyond 4.1 V originates from anionic activity, which induces an irreversible P2–O2 phase transition.[28] Notably, the intensity of this high-voltage couple diminishes and shifts to lower potentials from the 1st to the 4th cycle, indicating progressive and irreversible structural degradation. This instability is a primary contributor to the poor cycling performance of NNM at high voltages. In contrast, the CV profile of the NNMC10F10 sample (Fig. 3d) reveals that Cu/F co-doping effectively suppresses the anionic redox activity above 4.1 V, as evidenced by the near absence of the corresponding reduction peak. A new redox couple emerges at 3.86/3.85 V, which is characteristic of the Cu^{2+}/Cu^{3+} redox reaction.[29] The two pairs at 3.42/3.33 V and 3.64/3.54 V correspond to the Ni^{2+}/Ni^{3+} and Ni^{3+}/Ni^{4+} redox processes, respectively. Crucially, the first four CV cycles for the NNMC10F10 electrode exhibit significantly greater overlap compared to those of NNM. This superior electrochemical reversibility underscores the enhanced structural robustness and cycling stability imparted by co-doping, confirming its efficacy for high-voltage operation.

Fig. 3b and e present the galvanostatic charge–discharge profiles of NNM and NNMC10F10 within 2.0–4.4 V at 0.1C. Although the galvanostatic charge–discharge curves of NNMC10F10 exhibit an apparent plateau above 4.0 V, both the dQ/dV curves and *in situ* XRD confirm that this region actually corresponds to a quasi-plateau behavior associated with a solid-solution reaction, rather than a two-phase reaction. This

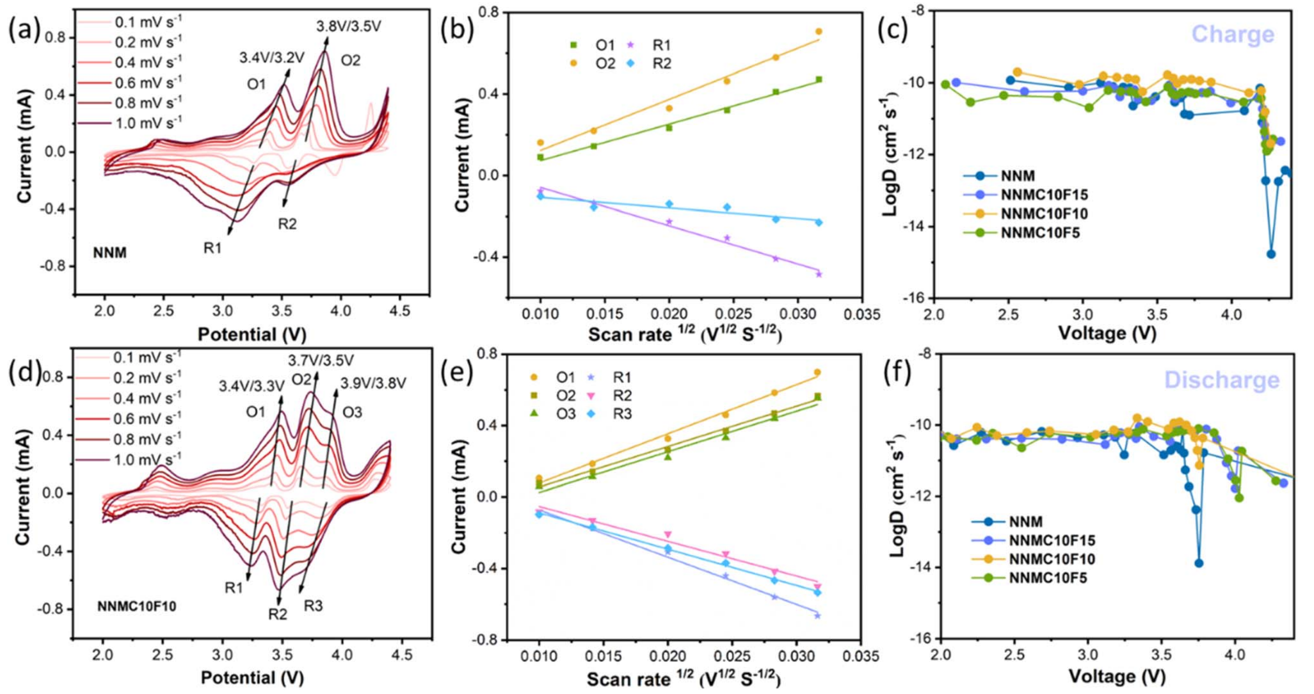

Fig. 4 CV curves at different scanning speeds (a) NNM and (d) NNMC10F10. The fitting curve between I_p and $V^{1/2}$ of (b) NNM and (e) NNMC10F10. (c) The diffusion rate of sodium ions during the charging process calculated by the GITT test for the four samples and (f) the diffusion rate of Na^+ during the discharge process.

phenomenon originates from the significant flattening of the voltage–sodium content relationship induced by Cu/F co-doping. The NNM electrode delivered an initial discharge capacity of 137.7 mA h g^{-1} with a first-cycle coulombic efficiency (CE) of 87.97%. In contrast, the NNMC10F10 electrode achieved a significantly higher initial discharge capacity of 139.6 mA h g^{-1} and a markedly improved first-cycle CE of 99.34%. The charge–discharge curves of NNMC10F10 show excellent overlap over the first five cycles, whereas those of NNM exhibit pronounced contraction, indicating severe capacity fading. After 50 cycles, the NNM electrode retained only 59.7% of its initial capacity (Fig. S5), whereas the NNMC10F10 electrode demonstrated significantly superior stability, maintaining 94.3% capacity retention (Fig. S6). This contrast suggests that NNM undergoes substantial irreversible oxygen redox activity, leading to rapid capacity decay, while co-doping with Cu and F effectively suppresses such irreversible processes. Fig. S7 showing SEM images of NNM and NNMC10F10 after 100 cycles at a voltage of 2–4.4 V and a current density of 1C. It can be observed that the materials retain a spherical morphology without cracks, further indicating that the spherical morphology effectively suppresses interfacial side reactions.

The differential capacity (d*Q*/d*V*) curves for the first three cycles are shown in Fig. 3c and f. For NNM, the peak above 4.1 V, associated with oxygen redox, diminishes sharply in intensity from the second cycle onward, indicating deteriorating reversibility. In comparison, the corresponding redox activity in NNMC10F10 remains stable, consistent with the CV results. Moreover, the voltage hysteresis between the oxidation and reduction peaks is smaller for NNMC10F10 than for NNM, further reflecting the improved electrochemical reversibility and structural stability of the co-doped material. Long-term cycling performance was evaluated at 1C (Fig. 3g). NNMC10F10 delivered an initial discharge capacity of 130.8 mA h g^{-1} and retained 88.07% of its capacity after 100 cycles, substantially outperforming NNM (48.96% retention). An optimal amount of F^- doping stabilizes the crystal structure, thereby enhancing both capacity and cycling stability. However, excessive F^- doping increases the Mn^{3+} content due to charge compensation, which can induce detrimental effects such as Jahn–Teller distortion. Rate capability tests were conducted at various current densities from 0.1C to 5C and then back to 0.1C (Fig. 3h). NNMC10F10 exhibited the highest discharge capacities at all rates, notably delivering 85.3 mA h g^{-1} at 5C, compared to only 47.9 mA h g^{-1} for NNM. Due to the strong electronegativity and non-oxidizable nature of fluorine, the substitution of oxygen by fluorine suppresses the anionic redox activity, thereby preventing oxygen loss and enhancing cycling stability. However, this comes at the cost of sacrificing part of the capacity contributed by anionic redox under high-rate charge–discharge conditions. Consequently, the improvement in capacity afforded by fluorine doping is less pronounced at high current densities than at low current densities. When the current was returned to 0.1C, the capacity of NNMC10F10 recovered to 130.3 mA h g^{-1}, demonstrating excellent reversibility and rapid Na^+ (de)intercalation kinetics.

To evaluate Na^+ diffusion kinetics, GITT measurements were performed. As shown in Fig. 4c and f, the NNMC10F10 electrode

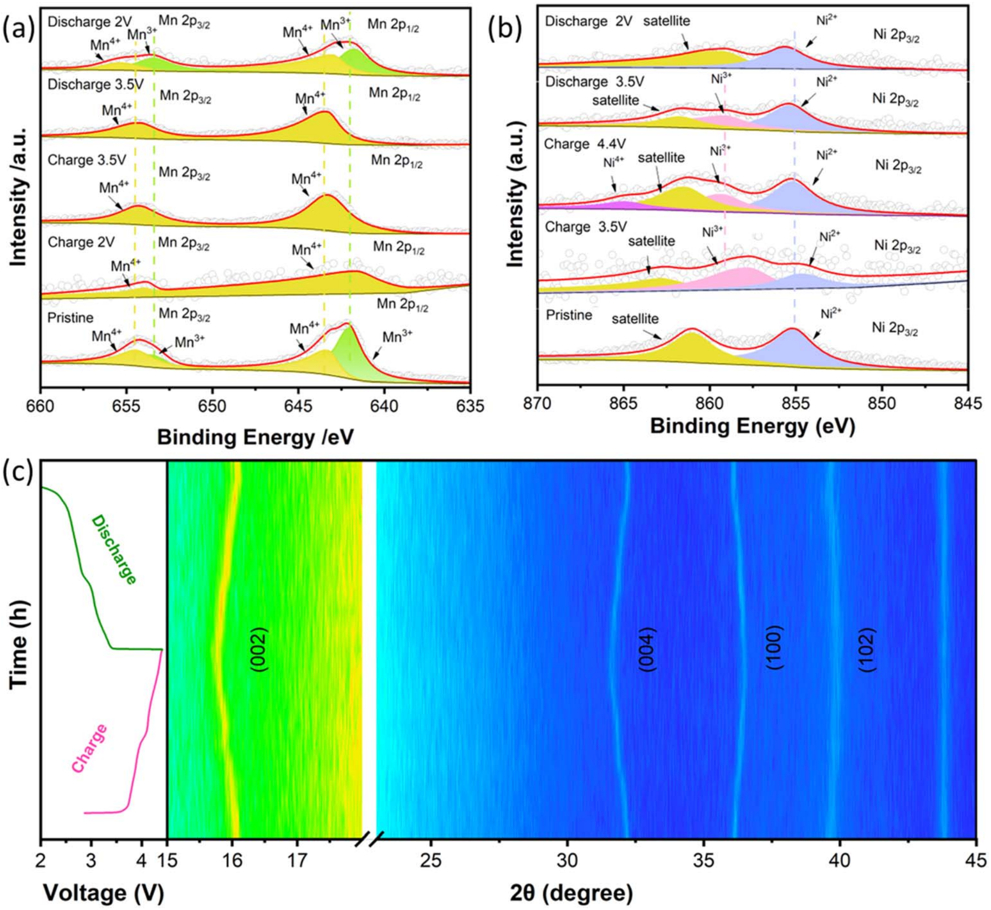

Fig. 5 *Ex situ* XPS tests of NNMC10F10 for (a) Mn 2p spectrum and (b) Ni 2p spectrum. (c) *In situ* XRD plots of NNMC10F10.

exhibits the highest Na^+ diffusion coefficient, in the range of 10^{-11}–10^{-9} cm^2 s^{-1}, which is substantially greater than that of NNM (10^{-15}–10^{-10} cm^2 s^{-1}). This result indicates superior ionic conductivity and rate capability for the co-doped material, consistent with the rate performance shown in Fig. 3h. Furthermore, the GITT voltage profile of NNM (Fig. S8a) displays a distinct plateau around 4.2 V, indicative of a two-phase P2–O2 transition. In contrast, the equilibrium voltage curve of NNMC10F10 (Fig. S8b) varies continuously, characteristic of a solid-solution reaction without a phase transformation.[30] Additionally, the GITT curves of NNM exhibit a trend of first sharply decreasing and then increasing. This behavior is attributed to the occurrence of Na^+/vacancy ordering when the voltage reaches a certain value, which forces Na^+ to overcome additional potential energy during hopping, leading to a marked decrease in the diffusion coefficient. As the voltage further increases, the vacancy concentration rises, the ordered structure is disrupted, the hopping barrier for Na^+ is lowered, and the diffusion coefficient recovers. CV was also conducted at various scan rates from 0.1 to 1 mV s^{-1} (Fig. 4a and d). With increasing scan rate, the peak currents rise accordingly while the CV profiles maintain their shape, suggesting favorable Na^+ insertion/extraction kinetics. The linear relationship between the peak current (I_p) and the square root of the scan rate ($V^{1/2}$) is plotted in Fig. 4b and e. Based on the Randles–Sevcik equation, the apparent Na^+ diffusion coefficients for the O1, O2, R1, and R2 peaks of NNM are calculated as 5.77×10^{-11}, 2.97×10^{-11}, 3.26×10^{-11}, and 2.47×10^{-12} cm^2 s^{-1}, respectively. For NNMC10F10, the corresponding values for the O1, O2, O3, R1, R2, and R3 peaks are 7.07×10^{-11}, 4.76×10^{-11}, 4.82×10^{-11}, 6.53×10^{-11}, 3.53×10^{-11}, and 3.86×10^{-11} cm^2 s^{-1}. These calculated diffusion coefficients align well with the trends observed in the GITT measurements.

The charge compensation mechanism in the NNMC10F10 electrode was probed using *ex situ* X-ray photoelectron spectroscopy (XPS) at different states of charge during galvanostatic cycling. Fig. S9 shows the XPS spectra of NNMC10F10 after a full charge–discharge cycle (charged to 4.4 V and then discharged to 2 V). No additional substances are observed, indicating the absence of side reactions. Fig. 5a displays the Mn 2p spectra of NNMC10F10. The peaks located at 642.06/653.52 eV and 643.25/654.44 eV are assigned to Mn^{3+} and Mn^{4+}, respectively.[31,32] Fig. S10 shows the XPS analysis of Mn for NNM and NNMC10F10. The Mn^{3+} content in NNM is 43.31%, while that in NNMC10F10 is 58.21%, demonstrating that F doping effectively increases the Mn^{3+} content. In the pristine state, NNMC10F10 shows a higher Mn^{3+}/Mn^{4+} ratio than NNM, indicating a lower average Mn oxidation state due to charge compensation

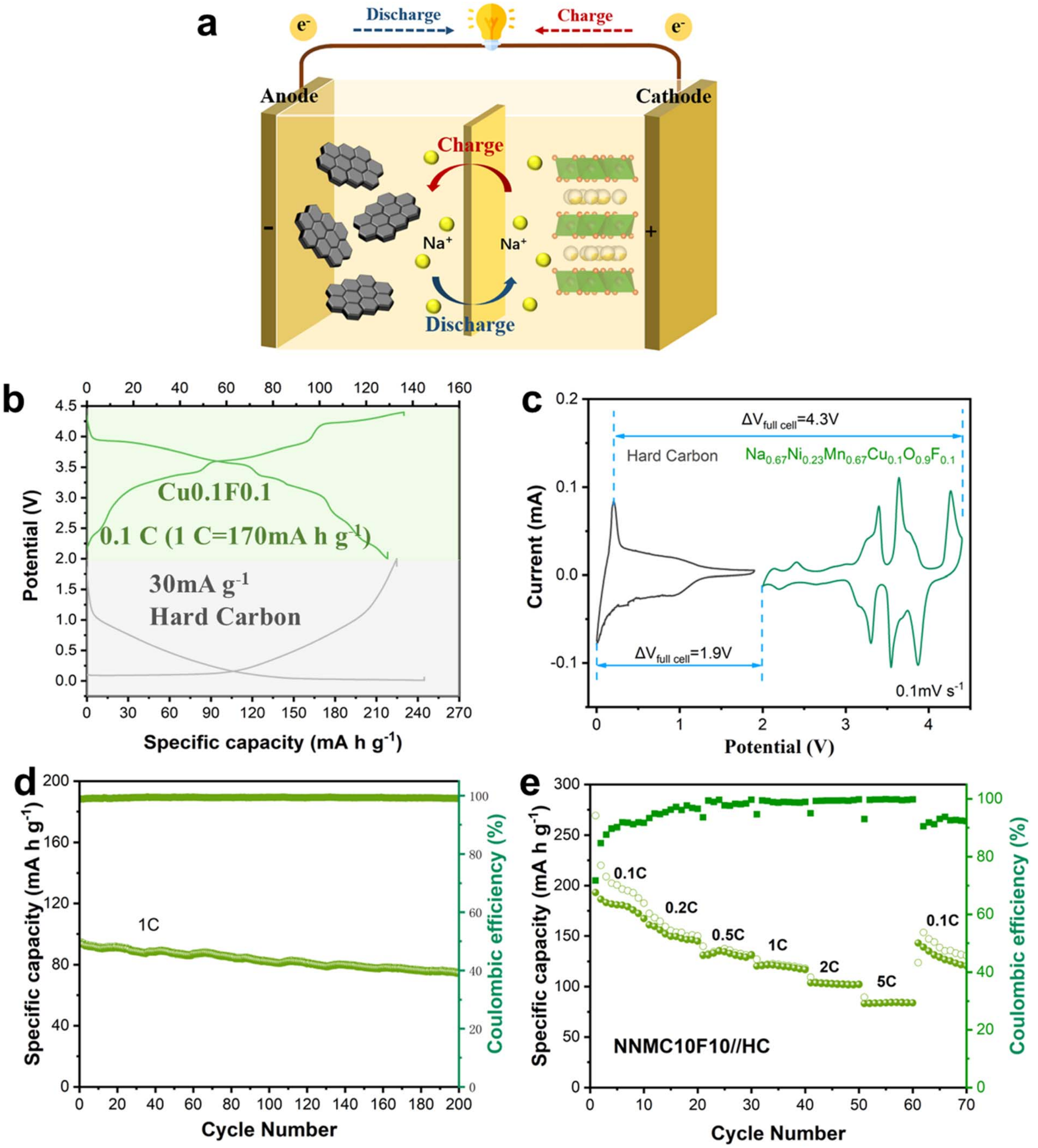

Fig. 6 (a) Configuration of the NNMC10F10 cathode//hard carbon anode full battery. (b) Galvanostatic charge–discharge profiles and (c) CV curves of the NNMC10F10 cathode and hard carbon anode. (d) Cycling lifespan of the full cell at 1C between 1.9–4.3 V. (e) Rate performance of the full cell between 1.9–4.3 V.

induced by Cu/F co-doping. Upon charging to 3.5 V, Mn^{3+} is fully oxidized to Mn^{4+}. During subsequent discharge to 2.0 V, a portion of Mn^{4+} is reversibly reduced back to Mn^{3+}. Compared with NNM, the Mn redox activity in NNMC10F10 is more pronounced and exhibits enhanced reversibility over the cycling window. Fig. 5b presents the Ni 2p spectra of NNMC10F10. The pristine electrode is dominated by Ni^{2+} (855.41 eV). Charging to 3.5 V partially oxidizes Ni^{2+} to Ni^{3+} (859.12 eV), and further charging to 4.4 V generates a small amount of Ni^{4+} (864.27 eV). Upon discharge to 2.0 V, all Ni species are reduced back to Ni^{2+}, confirming the high reversibility of the $Ni^{2+}/Ni^{3+}/Ni^{4+}$ redox couple.[33,34] In contrast, the Ni 2p spectrum of NNM (Fig. S11b) reveals an additional peak near 851 eV after charging, which is attributed to Ni ions migrating from the transition-metal layer into tetrahedral sites.[35]

In situ XRD was employed to monitor the structural evolution of the NNMC10F10 cathode during electrochemical cycling (Fig. 5c). Upon charging, the (002) and (004) diffraction peaks shift toward lower angles, reflecting an expansion of the interlayer spacing. This expansion is attributed to the increased electrostatic repulsion between adjacent oxygen layers as Na^+ ions are extracted. During the subsequent discharge process, all peaks shift back toward higher angles and return to their original positions by the end of the cycle, demonstrating highly reversible structural evolution. The co-doping of Cu^{2+} and F^- effectively suppresses irreversible phase transitions, thereby preserving the P2-type structure throughout the entire charge–discharge process. Fig. S12 shows the material exhibits a volume change of only 1.5%, an *a*-axis lattice parameter change of only 1.2%, and a *c*-axis lattice parameter change of only 0.9%. Which is lower than that of most reported cathode materials for sodium-ion batteries (Table S4).[36–41]

To assess the practical viability of the NNMC10F10 cathode, a full cell was assembled by coupling it with a commercial hard carbon (HC) anode, as illustrated in Fig. 6a. Prior to assembly, the HC anode was electrochemically preactivated by five galvanostatic cycles at a current density of 30 mA g^{-1}. The full cell was then constructed in a discharged state within an argon-filled glove box. To optimize the capacity balance between electrodes, the mass ratio of cathode to anode active materials was carefully adjusted to 1.3 : 1 (Fig. 6b). The operating voltage window of the full cell was established as 1.9–4.3 V based on CV analysis (Fig. 6c). The cell exhibited excellent cycling stability, maintaining a capacity retention of 87.38% after 100 cycles and 79.47% after 200 cycles at 1C within this voltage range (Fig. 6d). Fig. 6e shows the rate performance of the NNMC10F10//HC full cell. These results underscore the promising potential of the co-doped cathode material for practical sodium-ion battery applications.

4. Conclusions

This study presents a synergistic Cu/F co-doping strategy to significantly enhance the electrochemical performance of P2-type $Na_{0.67}Ni_{0.33}Mn_{0.67}O_2$ layered oxide cathodes for sodium-ion batteries. A series of copper-doped P2-$Na_{0.67}Ni_{0.33-x}Mn_{0.67}Cu_xO_2$ microspheres were first synthesized *via* a co-precipitation method. The unique spherical morphology contributes to improved cycling stability, while the incorporation of Cu^{2+} enhances the structural integrity of the cathode at high operating voltages. The NNMC10 delivered an initial discharge capacity of 118.8 mA h g^{-1} at 1C within 2.0–4.4 V and retained 80.64% of its capacity after 100 cycles. To further elevate capacity and long-term stability, secondary fluorine doping was introduced into the NNMC10 host matrix. Fluorine effectively stabilizes the crystal structure, yielding the final co-doped material, P2-$Na_{0.67}Ni_{0.23}Mn_{0.67}Cu_{0.1}O_{0.9}F_{0.1}$ microspheres, which exhibit superior electrochemical properties. The co-doped cathode achieved an initial capacity of 130.8 mA h g^{-1} at 1C with a capacity retention of 88.07% after 100 cycles. Notably, it delivered a high specific capacity of 139.6 mA h g^{-1} at 0.1C and maintained 85.3 mA h g^{-1} even at a high rate of 5C. In the future, it will be necessary to employ techniques such as synchrotron-based soft X-ray absorption spectroscopy (soft XAS) and resonant inelastic X-ray scattering (RIXS) to quantitatively integrate the reversible/irreversible oxygen redox activity and the variation in the Mn^{3+}/Mn^{4+} ratio, thereby establishing a precise model of the contributions of beneficial evolution and detrimental degradation to capacity. This combined modification approach simultaneously mitigates undesirable interfacial side reactions and reinforces the structural framework, effectively suppressing irreversible oxygen redox activity and phase transitions during cycling. The findings offer valuable insights for the rational design of high-performance layered oxide cathodes for advanced sodium-ion batteries.

Conflicts of interest

The authors declare that there are no conflicts of interest regarding the publication of this paper.

Data availability

All data generated or analyzed during this study are included in this article (and its supplementary information (SI) files). Supplementary information is available. See DOI: https://doi.org/10.1039/d6ta00731g.

References

1 J. Wang, Y. F. Zhu, Y. Su, J. X. Guo, S. Chen, H. K. Liu, S. X. Dou, S. L. Chou and Y. Xiao, Routes to high-performance layered oxide cathodes for sodium-ion batteries, *Chem. Soc. Rev.*, 2024, **53**, 4230.

2 H. Yang, D. Wang, Y. Liu, B. Zhong, Y. Song, Q. Kong, Z. Wu and X. Gou, Improvement of cycle life for layered oxide cathodes in sodium-ion batteries, *Energy Environ. Sci.*, 2024, **17**, 1756–1780.

3 L. Sun, J. Zeng, X. Wan, C. Peng, J. Wang, C. Lin, M. Zhu and J. Liu, Recent progress of interface modification of layered oxide cathode material for sodium-ion batteries, *Electron*, 2024, **2**, e31.

4 Z. Chen, Y. Deng, J. Kong, W. Fu, F. Liu, T. Jin and L. Jiao, Toward the High-Voltage Stability of Layered Oxide Cathodes for Sodium-Ion Batteries: Challenges, Progress, and Perspectives, *Adv. Mater.*, 2024, **36**, 2402008.

5 P. T. Nguyen and T. I. Kim, Recent Advances in Sodium-Ion Batteries: Cathode Materials, *Materials*, 2023, **16**, 6869.

6 Q. Zhao, S. X. Dou, H. K. Liu, H. Hu, L. Zhou and M. Chen, Recent progress and advances of high-entropy polyanionic cathodes in lithium-ion and sodium-ion batteries, *Chem. Commun.*, 2025, **61**, 12419–12430.

7 J. Hu, W. Zhao, Y. Wang, S. Jiang, B. Yu, S. X. Dou, H. K. Liu, S. Chen, K. Zhang, L. Zhou and M. Chen, The Role of Fluorine in Polyanionic Cathode Materials for Sodium-Ion Batterie, *Small Methods*, 2025, **9**, 7.

8 B. Zhou, Y. Gao, X. Lin, B. Yang, N. Kang, Y. Qiao, H. Zhang, L. Li and S. Chou, Bulk and interface engineering of Prussian blue analogue cathodes for high-performance sodium-ion batteries, *Chem. Sci.*, 2025, **16**, 13594–13628.

9 Y. Wang, Z. Sun, J. Zhu, F. Ye, J. Zhu, R. Li and G. Chang, A highly efficient chelating agent assisted the synthesis of Prussian blue analogues as a cathode material for sodium ion batteries, *Colloids Surf., A*, 2025, **716**, 136690.

10 T. Chen, J. Wang, B. Tan, K. Zhang, H. Banda, Y. Zhang, D. Kim and M. Dinca, High-Energy, High-Power Sodium-Ion Batteries from a Layered Organic Cathode, *J. Am. Chem. Soc.*, 2025, **147**(7), 6181–6192.

11 L. Cheng, X. Yang, J. Yu, X. Zhang, H. G. Wang, F. Cui and Y. Wang, Redox-Bipolar Covalent Organic Framework Cathode for Advanced Sodium-Organic Batteries, *Adv. Mater.*, 2024, **37**(1), e2411625.

12 T. Zhang, Y. Li, Z. Song, Y. Huang, F. Li, S. Cheng and F. Li, Insights into chemical-mechanical degradation and modification strategies of layered oxide cathode materials of sodium ion batteries, *J. Energy Chem.*, 2025, **103**, 294–315.

13 W. Zou, A. Innocenti, M. Zarrabeitia, D. Bresser, Y. Yang and S. Passerini, Layered Oxide Cathodes for Sodium-Ion Batteries: Storage Mechanism, Electrochemistry, and Techno-economics, *Acc. Chem. Res.*, 2023, **56**, 284–296.

14 L. Chang, R. Yang, X. Bi, W. Yang, K. Cai, A. Wei and J. Liu, Research progress of layered P2-$Na_{2/3}Ni_{1/3}Mn_{2/3}O_2$ cathode material for sodium ion batteries, *J. Energy Storage*, 2023, **73**, 109025.

15 Z. C. Jian, J. X. Gou, Y. F. Liu, Y. F. Zhu, J. Wang and Y. Xiao, Cation migration in layered oxide cathodes for sodium-ion batteries: fundamental failure mechanisms and practical modulation strategies, *Chem. Sci.*, 2024, **15**, 19698–19728.

16 M. Jiang, G. Qian, X. Z. Liao, Z. Ren, Q. Dong, D. Meng, G. Cui, S. Yuan, S. J. Lee, T. Qin, X. Liu, Y. Shen, Y. S. He, L. Chen, Y. Liu, L. Li and Z. F. Ma, Revisiting the capacity-fading mechanism of P2-type sodium layered oxide cathode materials during high-voltage cycling, *J. Energy Chem.*, 2022, **69**, 16–25.

17 C. Zheng, S. He, J. Gan, Z. Wu, L. She, Y. Gao, Y. Yang, J. Lou, Z. Ju and H. Pan, Scientific challenges faced by Mn-based layered oxide cathodes with anionic redox for sodium-ion batteries, *Carbon Energy*, 2025, **7**, e605.

18 L. Gao, S. Chen, H. Hu, H. Cheng, L. Zhang and X. Yang, Hierarchical NaxCoO2 microspheres with low surface area toward high performance sodium ion batteries, *Mater. Lett.*, 2020, **260**, 126965.

19 Y. Fang, X. Yu and X. Lou, A Practical High-Energy Cathode for Sodium-Ion Batteries Based on Uniform P2-$Na_{0.7}CoO_2$ Microspheres, *Angew. Chem., Int. Ed.*, 2017, **56**, 5801–5805.

20 X. Cui, S. Wang, X. Ye, X. Fan, C. Gao, Y. Quan, S. Wen, X. Cai, J. Huang and S. Li, Insights into the improved cycle and rate performance by ex-situ F and in-situ Mg dual doping of layered oxide cathodes for sodium-ion batteries, *Energy Storage Mater.*, 2022, **45**, 1153–1164.

21 A. Anilkumar, N. Nair, S. V. Nair and S. Baskar, Tailoring high Na content in P2-type layered oxide cathodes via Cu-Li dual doping for sodium-ion batteries, *J. Energy Storage*, 2023, **72**, 108291.

22 L. Wang, Y. G. Sun, L. L. Hu, J. Y. Piao, J. Gou, A. Manthiram, J. Ma and A. M. Cao, Copper-substituted $Na_{0.67}Ni_{0.3\text{-}x}Cu_xMn_{0.7}O_2$ cathode materials for sodium-ion batteries with suppressed P2 - O2 phase transition, *J. Mater. Chem. A*, 2017, **5**, 8752.

23 W. Kang, Z. Zhang, P. Lee, T. Ng, W. Li, Y. Tang, L. C. Zhang and D. Yu, Copper substituted P2-type $Na_{0.67}Cu_xMn_{1-x}O_2$: a stable high-power sodium-ion battery cathode, *J. Mater. Chem. A*, 2015, **3**, 22846.

24 Q. Zhang, Y. Huang, Y. Liu, S. Sun, K. Wang, Y. Li, X. Li, J. Han and Y. Huang, F-doped O3-$NaNi_{1/3}Fe_{1/3}Mn_{1/3}O_2$ as high-performance cathode materials for sodium-ion batteries, *Sci. China Mater.*, 2017, **60**(7), 629–636.

25 X. Song, R. Liu, J. Jin, X. Zhao, Y. Wang, Q. Shen, Z. Sun, X. Qu, L. Jiao and Y. Liu, Unraveling the functioning mechanism of fluorine-doping in Mn-based layered oxide cathodes toward enhanced sodium-ion storage performance, *Energy Storage Mater.*, 2024, **69**, 103377.

26 Y. Yang, C. Wu, X. X. He, J. Zhao, Z. Yang, L. Li, X. Wu, L. Li and S. L. Chou, Boosting the Development of Hard Carbon for Sodium-Ion Batteries: Strategies to Optimize the Initial Coulombic Efficiency, *Adv. Funct. Mater.*, 2024, **34**, 2302277.

27 Y. Xiao, Y. F. Zhu, H. R. Yao, P. F. Wang, X. D. Zhang, H. Li, X. Yang, L. Gu, Y. C. Li, T. Wang, Y. X. Yin, X. D. Guo, B. H. Zhang and Y. D. Gou, A Stable Layered Oxide Cathode Material for High-Performance Sodium-Ion Battery, *Adv. Energy Mater.*, 2019, **9**, 1803978.

28 X. Chen, C. Wang, Y. Zhao, Y. Wang, X. Yin and N. Zhang, Recent progress in layered oxide cathodes for sodium-ion batteries: stability, phase transition and solutions, *J. Mater. Chem. A*, 2024, **12**, 31797.

29 J. Wang, H. Liu, Q. Yang, B. Hu, F. Geng, C. Zhao, Y. Lin and B. Hu, Cu-Doped P2-$Na_{0.7}Mn_{0.9}Cu_{0.1}O_2$ Sodium-Ion Battery Cathode with Enhanced Electrochemical Performance: Insight from Water Sensitivity and Surface Mn (II) Formation Studies, *ACS Appl. Mater. Interfaces*, 2020, **12**, 34848–34857.

30 X. Wang, X. Yin, X. Feng, Y. Li, X. Dong, Q. Shi, Y. Zhao and J. Zhang, Rational design of $Na_{0.67}Ni_{0.2}Co_{0.2}Mn_{0.6}O_2$ microsphere cathode material for stable and low temperature sodium ion storage, *Chem. Eng. J.*, 2022, **428**, 130990.

31 T. Y. Yu and Y. K. Sun, A fluorinated O3-type layered cathode for long-life sodium-ion batteries, *J. Mater. Chem. A*, 2022, **10**, 23639.

32 Y. Zhang, G. Liu, C. Su, G. Liu, H. Sun, D. Qiao and L. Wen, Study on the influence of Cu/F dual-doping on the Fe-Mn based compound as cathode material for sodium ion batteries, *J. Power Sources*, 2022, **536**, 231511.

33 Z. X. Huang, K. Li, J. M. Cao, K. Y. Zhang, H. H. Liu, J. Z. Gou, Y. Liu, T. Wang, D. Dai, X. Y. Zhang, H. Geng and X. L. Wu, New Insights into Anionic Redox in P2-Type Oxide Cathodes for Sodium-Ion Batteries, *Nano Lett.*, 2024, **24**(43), 13615–13623.

34 C. Wu, Y. Xu, J. Song, Y. Hou, S. Jiang, R. He, A. Wei and Q. Tan, Research progress on P2-type layered oxide cathode materials for sodium-ion batteries, *Chem. Eng. J.*, 2024, **500**, 157264.

35 J. L. Shi, J. N. Zhang, X. D. Zhang, Y. X. Yin, H. Li, Y. G. Gou, L. Gu and L. J. Wan, Mitigating Voltage Decay of Li-Rich

Cathode Material via Increasing Ni Content for Lithium-Ion Batteries, *ACS Appl. Mater. Interfaces*, 2016, **8**(31), 20138–20146.

36 S. H. Jeong, I. K. Kim, S. Eom, H. Hwang, Y. H. Jung and J. H. Kim, Engineering the local chemistry through fe substitution in layered P2-$Na_{0.7}Ni_{0.2}Co_{0.2}Mn_{0.6}O_2$ for high-performance Sodium-Ion batteries, *Energy Storage Mater.*, 2025, **75**, 104041.

37 S. Yin, Z. Tao, Y. Zhang, X. Zhang, L. Yu, F. Ji, X. Ma, G. Yuan and G. Zhang, Constructing a Size-Controllable Spherical P2-Type Layered Oxides Cathode That Achieves Practicable Sodium-Ion Batteries, *ACS Appl. Mater. Interfaces*, 2024, **16**, 26340–26347.

38 L. Yang, X. Li, J. Liu, S. Xiong, X. Ma, P. Liu, J. Bai, W. Xu, Y. Tang, Y. Y. Hu, M. Liu and H. Chen, Lithium-Doping Stabilized High-Performance P2- $Na_{0.66}Li_{0.18}Fe_{0.12}Mn_{0.7}O_2$ Cathode for Sodium Ion Batteries, *J. Am. Chem. Soc.*, 2019, **141**(16), 6680–6689.

39 X. Zhang, F. Qiu, K. Jiang, P. He, M. Han, S. Gou and H. Zhou, Improving the structural and cyclic stabilities of P2-type $Na_{0.67}MnO_2$ cathode material via Cu and Ti co-substitution for sodium ion batteries, *Chem. Commun.*, 2020, **56**, 6293.

40 J. Z. Gou, P. F. Wang, X. L. Wu, X. H. Zhang, Q. Yan, H. Chen, J. P. Zhang and Y. G. Gou, High-Energy/Power and Low-Temperature Cathode for Sodium-Ion Batteries: In Situ XRD Study and Superior Full-Cell Performance, *Adv. Mater.*, 2017, **29**, 1701968.

41 F. Xia, D. Tie, J. Wang, H. Song, W. Wen, X. Ye, J. Wu, Y. Hou, X. Lu and Y. Zhao, Ultrahigh rate and durable sodium-ion storage at a wide potential window via lanthanide doping and perovskite surface decoration on layered manganese oxides, *Energy Storage Mater.*, 2021, **42**, 209–218.